

# TiO<sub>2</sub> Nanosheet Supported MnCeO<sub>x</sub>: A Remarkable Catalyst with Enhanced Low-Temperature Catalytic Activity in *o*-DCB Oxidation

**Xu He**

Hebei University of Technology

**Haiwei Guo**

Hebei University of Technology

**Xiaoyao Liu**

Hebei University of Technology

**Jiaxin Wen**

Hebei University of Technology

**Gengbo Ren**

Hebei University of Technology

**Xiaodong Ma** (✉ [maxd@hebut.edu.cn](mailto:maxd@hebut.edu.cn))

Hebei University of Technology

---

## Research Article

**Keywords:** TiO<sub>2</sub> nanosheet, MnCeO<sub>x</sub>/TiO<sub>2</sub>, Polychlorinated aromatic hydrocarbons, Catalytic oxidation, *o*-dichlorobenzene, Morphology engineering

**Posted Date:** February 15th, 2022

**DOI:** <https://doi.org/10.21203/rs.3.rs-1210140/v1>

**License:**   This work is licensed under a Creative Commons Attribution 4.0 International License.

[Read Full License](#)

---

**Version of Record:** A version of this preprint was published at Environmental Science and Pollution Research on April 23rd, 2022. See the published version at <https://doi.org/10.1007/s11356-022-20065-9>.

# Abstract

Morphology engineering was an effective strategy for 1,2-dichlorobenzene (*o*-DCB) oxidation. Herein, TiO<sub>2</sub> nanosheet supported MnCeO<sub>x</sub> (TiMn15Ce30-NS) showed excellent catalytic activity with T<sub>50%</sub> = 156 °C and T<sub>90%</sub> = 238 °C, which was better than the T<sub>50%</sub> = 213 °C and T<sub>90%</sub> = 247 °C for TiO<sub>2</sub> nano truncated octahedron supported MnCeO<sub>x</sub> (TiMn15Ce30-NTO). TiMn15Ce30-NS also exhibited enhanced water resistance (T<sub>50%</sub> = 179 °C, T<sub>90%</sub> = 240 °C), and good stability with the *o*-DCB conversion retained at 98.9% for 12 h at 350 °C. The excellent catalytic activity of TiMn15Ce30-NS could be mainly ascribed to the preferentially exposed {001} crystal plane which favored the higher concentration of Mn<sup>4+</sup> along with surface active oxygen, as well as stronger interaction between MnO<sub>x</sub> and CeO<sub>x</sub> in TiMn15Ce30-NS. The present results deepen the understanding of the morphology-dependent effect on *o*-DCB oxidation.

## 1. Introduction

The effective removal of polychlorinated aromatic hydrocarbons (PCAHS) originated from the waste incinerating process has received a widespread concern for the pollutants could result in serious damage to the health of humanity and the eco-environment (He et al. 2019a). Catalytic oxidation has been deemed as a promising approach for PCAHS abatement for its low reaction temperature, satisfied degradation performance, and harmless products (Zhang et al. 2018) compared with the generally used methods such as heat treatment (Lindberg et al. 2015) and physical adsorption (Li et al. 2016). The key issue for decomposing PCAHS is to develop catalysts with high efficiency.

Transition metal oxides such as CeO<sub>x</sub> (Long et al. 2019), FeO<sub>x</sub> (Ma et al. 2014), CrO<sub>x</sub> (Deng et al. 2021), CuO<sub>x</sub> (He et al. 2019b), and MnO<sub>x</sub> (Qiu et al. 2021) have drawn extraordinary interest for the cost advantage and their strong resistance to chlorine poisoning compared with noble metals which are costly and prone to poison by chlorine species during the catalysis process (van den Brink et al. 2000). In particular, MnO<sub>2</sub> exhibited good reducibility and catalytic activity in PCAHS oxidation among various transition metal oxides (Weng et al. 2019). In addition, the catalytic activity of MnO<sub>2</sub> could be further improved through doping CeO<sub>2</sub> with high oxygen storage capacity (Li et al. 2019a, Li et al. 2018). MnCeO<sub>x</sub>-based catalysts have been prepared for PCAHS oxidation (Chen et al. 2019), while the current catalysts showed two main drawbacks: i) high oxidation temperature. For example, MnO<sub>x</sub>/CeO<sub>2</sub> bimetal oxides MnCe (0.43) showed an unsatisfactory catalytic performance for chlorobenzene combustion with the temperature with 90% conversion (T<sub>90%</sub>) of 279 °C (Wu et al. 2017). ii) poor water resistance. e.g., Sun et al. (Sun et al. 2016) reported that the Mn<sub>0.8</sub>Ce<sub>0.2</sub>O<sub>2</sub> showed a severe deactivation in the presence of water due to its competitive adsorption when the temperature was higher than 250 °C. Thus, the further modification of MnCeO<sub>x</sub>-based catalysts to improve the low-temperature catalytic performance along with water resistance for PCAHS oxidation is highly required.

TiO<sub>2</sub> has been used as supports in catalytic oxidation (Liu et al. 2001). Recently, researchers have found that catalytic performance of TiO<sub>2</sub> supported catalysts could be modulated through morphology engineering (Wen et al. 2021), which could affect the interface adsorption and reaction centers (Khan et al. 2020). TiO<sub>2</sub> with certain morphology also affected the Lewis acid strength of the catalyst through the geometric arrangement of the surface O<sup>2-</sup> ligands (Martra 2000). Therefore, morphology engineering of TiO<sub>2</sub> could be used as a strategy for promoting the interaction between the active components and the carrier (Wen et al. 2021), improving the catalytic activity of the catalyst. Our previous study showed that TiFe<sub>5</sub>Ca<sub>70</sub>-S designed by morphology-engineering demonstrated better catalytic activity for *o*-DCB oxidation with the T<sub>90%</sub> of 322 °C (Wen et al. 2021), while the low temperature catalytic activity required further improvement. Researchers have also shown that the behavior of H<sub>2</sub>O on TiO<sub>2</sub> could be adjusted through facets design (Vittadini et al. 1998), and whether the water resistance in PACHs oxidation could be enhanced through morphology design is another interesting project. Moreover, the detailed oxidation mechanism of *o*-DCB over the catalysts with certain facet still needs investigation.

Motivated by the above discussion, we attempted to synthesize the catalyst with improved low-temperature catalytic activity and water resistance through morphology-engineering. Herein, TiO<sub>2</sub> catalysts with different morphologies, namely TiO<sub>2</sub> nanosheet (TiO<sub>2</sub>-NS) and TiO<sub>2</sub> nano truncated octahedron (TiO<sub>2</sub>-NTO) were prepared via hydrothermal treatment. Subsequently, the supported MnCeO<sub>x</sub>/TiO<sub>2</sub> catalysts (TiMn<sub>15</sub>Ce<sub>y</sub>-NS and TiMn<sub>15</sub>Ce<sub>y</sub>-NTO) were used for the catalytic oxidation activity of *o*-DCB (a PCAHs model compound). The relationship between catalytic activity and the morphology of TiMnCe was investigated. In addition, the reaction mechanism of *o*-DCB on MnCeO<sub>x</sub>/TiO<sub>2</sub>-NS was also explored by in situ diffuse reflectance infrared Fourier transform spectroscopy (in situ DRIFT).

## 2. Experimental

### 2.1. Catalyst preparation

TiO<sub>2</sub>-NS and TiO<sub>2</sub>-NTO were hydrothermally synthesized in this paper. The MnO<sub>x</sub>/TiO<sub>2</sub>, and MnCeO<sub>x</sub>/TiO<sub>2</sub> were subsequently prepared by the impregnation method. The experimental details were illustrated in Supporting Information.

### 2.2. Catalyst characterization

Catalyst characterizations of TiO<sub>2</sub>-NS, TiO<sub>2</sub>-NTO, MnO<sub>x</sub>/TiO<sub>2</sub>, and MnCeO<sub>x</sub>/TiO<sub>2</sub> such as X-ray diffraction (XRD), the scanning electron microscopy (SEM), Transmission electronic microscopy (TEM) and the high resolution transmission electron microscope (HRTEM), H<sub>2</sub> temperature-programmed reduction (H<sub>2</sub>-TPR), X-ray photoelectron spectroscopy (XPS) and in-situ DRIFT, etc. are described in the Supporting Information.

## 2.3. Catalyst evaluation

In this work, the catalytic oxidation of *o*-DCB was evaluated in a continuous-flow fixed-bed microreactor. During the catalytic evaluation process, the mixed gas (10% O<sub>2</sub>, 90% N<sub>2</sub>) was divided into two paths, one path flowed through the *o*-DCB saturated vapor to carry *o*-DCB, and the other path gas was regarded as balance gas. And the third water path (0.5 vol.% water vapor) would be added when the experiment was carried out with the presence of water. The two paths of gas were then fully mixed again. Subsequently, the mixed reaction gas consisting of 50 ppm *o*-DCB flowed through the fixed catalytic bed reactor with a total flow rate of 60 mL/min. After the catalytic reaction in the reactor, *o*-DCB in effluent gas was detected using GC1100 gas chromatography with FID detector. The catalytic properties were expressed with the conversion of *o*-DCB, which was calculated by the following equation,

$$X(\%) = \frac{C_1 - C_2}{C_1} \times 100\% \quad (1)$$

Where  $C_1$  is the initial concentration of *o*-DCB,  $C_2$  is the final concentration after the catalytic reaction.

## 3. Results And Discussion

### 3.1. Catalysts Characterization

Figure 1 presented SEM images of TiO<sub>2</sub>-NS and TiO<sub>2</sub>-NTO and HRTEM images of TiMn15Ce30-NS and TiMn15Ce30-NTO. As shown in Fig. 1a, TiO<sub>2</sub>-NS presented a nanosheet-like morphology with 70 ~ 160 nm in length, and TiO<sub>2</sub>-NTO presented a truncated bipyramid with the edge length of the upper and lower planes of the bipyramid was about 30 ~ 100 nm (Fig. 1b). HRTEM image of TiMn15Ce30-NS in Fig. 1c showed the lattice spacing of 0.24 and 0.35 nm which could be assigned to the interplanar distances of the {001} plane and {101} plane of anatase phase TiO<sub>2</sub> (Wang et al. 2020b).

Combined the SEM and HRTEM analysis, we presented schematic diagrams of TiMn15Ce30-NS in Fig. 1e, and the flat top and bottom surfaces should be the {001} planes based on the symmetries of anatase TiO<sub>2</sub> (Li et al. 2019b), indicating the preferential exposed {001} plane of TiMn15Ce30-NS catalyst. Similarly, the lattice fringes of 0.36 nm corresponded to the {101} plane for the TiO<sub>2</sub> in TiMn15Ce30-NTO (Fig. 1d) (Leng et al. 2015) and we concluded that TiMn15Ce30-NTO preferentially exposed {101} plane which could be presented as the schematic diagrams in Fig. 1f.

Besides, the nanosheet-like and truncated bipyramid morphology were mainly retained in TiMn15Ce30-NS (Fig. S1a) and TiMn15Ce30-NTO (Fig. S1b) and uniformly distributed particles were also observed on the surface due to the addition of Mn and Ce. Energy spectrum scanning of TiMn15Ce30-NS revealed that four elements including Mn, Ce, O and Ti were detected on the surface of the catalyst (Fig. 2), demonstrating that Mn and Ce were successfully supported on TiO<sub>2</sub> nanosheet. The Mn and Ce were

dispersed evenly on the surface of the carrier, which is conducive to improving the catalytic activity (Jiao et al. 2019).

The XRD patterns of anatase  $\text{TiO}_2$ -NS,  $\text{TiO}_2$ -NTO, TiMn15Ce30-NS and TiMn15Ce30-NTO were presented in Fig. 3, and the results showed that the peaks of  $\text{TiO}_2$ -NTO and  $\text{TiO}_2$ -NS were consistent with the anatase phase  $\text{TiO}_2$  (JCPDS 21-1272) (Gui et al. 2009). After loading Mn, the corresponding peaks of TiMn15-NS did not change significantly (Fig. S2). With the loading of Ce in TiMn15-NS, the peak at  $28.9^\circ$  attributing to  $\text{MnO}_2$  (110) (JCPDS 24-0735) crystal plane was observed (Cao et al. 2017). The average crystal sizes of  $\text{TiO}_2$ -NS,  $\text{TiO}_2$ -NTO, TiMn15Ce30-NS and TiMn15Ce30-NTO were calculated by Scherrer equation based on the (101) diffraction peak of  $\text{TiO}_2$  (Table S1). Noticeably, the grain size was 43.8 nm in  $\text{TiO}_2$ -NS, and the value reduced to 34.2 nm in TiMn15Ce30-NS, demonstrating the crystal size of  $\text{TiO}_2$  was refined by introducing Mn and Ce. While the counterpart data in TiMn15Ce30-NTO increased to 40.0 nm from 37.9 nm in  $\text{TiO}_2$ -NTO. It is well-known that smaller grain size endows more abundant surface area or interface area, which might provide more defect sites as active sites for catalytic reactions, promoting catalytic activity (Zhao et al. 2020b).

Deng et al. (Deng et al. 2016) have proved that the preferential exposure of the (001) crystal plane of  $\text{TiO}_2$  crystal was related to the broad peak of the (004) diffusion and the narrower peak of (200). As can be seen in Table S1, the full width at half maximum (FWHM) of TiMn15Ce30-NS (004) ( $0.312^\circ$ ) peak was larger than that of TiMn15Ce30-NTO ( $0.192^\circ$ ), while its FWHM of (200) peak ( $0.223^\circ$ ) was smaller than the corresponding data of  $0.227^\circ$  for TiMn15Ce30-NTO. This phenomenon further proved that TiMn15Ce30-NS preferentially exposed {001} crystal plane as obtained in Fig. 1.

Figure 4 depicted the  $\text{N}_2$  adsorption/desorption isothermal of pure  $\text{TiO}_2$ , TiMn15-NS and TiMn15Ce30-NS.  $\text{TiO}_2$ -NS showed I-type isotherm (IUPAC) (Rahman et al. 2019) and its curve increased slightly in the relative pressure ranging from 0.0 to 0.2 ascribed to micropores filling (Abebe et al. 2018), implying that the pore structure of  $\text{TiO}_2$ -NS was mainly microporous. The TiMn15-NS was presented as a type IV isotherm and it displayed an H3-type hysteresis loop at relative pressure from 0.75 to 1.0, besides, the rapid rise during the relative pressure from 0.85 to 1.0 might be attributed to the condensation of adsorbate gas (Abebe et al. 2018). After the introduction of Ce, the isotherm of TiMn15Ce30-NS retained type IV, and the H3-type hysteresis loop appeared at  $P/P_0$  of 0.7 ~ 1.0.

Table 1 summarized the specific surface area and average pore diameter of catalysts. The average pore size of  $\text{TiO}_2$ -NS was 1.41 nm, and the value was 7.83 nm in TiMn15-NS, indicating that TiMn15-NS mainly possessed mesoporous. Moreover, the specific surface area of TiMn15-NS was  $32.0 \text{ m}^2/\text{g}$  comparing to the  $19.8 \text{ m}^2/\text{g}$  in  $\text{TiO}_2$ -NS attributed to the loading of Mn. The specific surface area of TiMn15Ce30-NS did not change significantly after further loading Ce, while TiMn15Ce30-NS presented a hierarchical porous structure with a relatively wide pore distribution at 8.78, 17.63, and 36.51 nm ranging from 2 ~ 86 nm (Fig. 3), indicating the coexistence of mesoporous and macroporous. Studies have

reported that the mesoporous structure could provide relatively higher internal specific surface area (Liu & He 2010), and the macroporous possessed relatively small diffusion resistance, which is conducive to the mass transfer process (Arandiyana et al. 2018). Thereby, we could reasonably deduce that the wide range of hierarchical porous structure of TiMn15Ce30-NS may be favorable for  $\sigma$ -DCB diffusion and adsorption on TiMn15Ce-NS, promoting the catalytic oxidation activity.

Table 1

Surface areas, total pore volumes and average pore diameters of TiO<sub>2</sub>-NS, TiMn15-NS and TiMn15Ce30-NS.

Samples	S <sub>BET</sub> [a] (m <sup>2</sup> /g)	V <sub>p</sub> [a] (cm <sup>3</sup> /g)	D <sub>p</sub> [a] (nm)
TiO <sub>2</sub> -NS	19.8	0.05	1.41
TiMn15-NS	32.0	0.06	7.83
TiMn15Ce30-NS	32.0	0.07	6.83

[a] Structure parameters of the catalysts calculated via N<sub>2</sub> isotherm; S<sub>BET</sub>: BET surface area; V<sub>p</sub>: total pore volume; D<sub>p</sub>: average pore diameter.

The reduction performances of TiO<sub>2</sub>-NS, TiMn15-NS and TiMn15Ce30-NS were studied through H<sub>2</sub>-TPR with the results reflected in Fig. 5. The reduction temperature of pristine TiO<sub>2</sub>-NS was 658 °C. After loading Mn on the TiO<sub>2</sub>-NS, the reduction temperature of TiO<sub>2</sub> in TiMn15-NS decreased to 636 °C. In addition, two new reduction peaks centered at 265 °C assigned to the reduction of MnO<sub>2</sub> to Mn<sub>2</sub>O<sub>3</sub> and 335 °C attributed to the transformation of Mn<sub>2</sub>O<sub>3</sub> to Mn<sub>3</sub>O<sub>4</sub> were observed (Chen et al. 2018). The peak at 447 °C can be attributed to the reduction of Mn<sub>3</sub>O<sub>4</sub> to MnO (Zhao et al. 2019). For TiMn15Ce30-NS, the temperature of MnO<sub>2</sub> to Mn<sub>2</sub>O<sub>3</sub> and Mn<sub>2</sub>O<sub>3</sub> to Mn<sub>3</sub>O<sub>4</sub> decreased to 236 °C and 297 °C, respectively. The peak attributed to Mn<sub>3</sub>O<sub>4</sub> reduction to MnO was also reduced to 396 °C on the TiMn15Ce30-NS curve (Wu et al. 2019). These results revealed that the addition of Ce significantly affected the reduction temperatures of MnO<sub>x</sub>, proving that the loading of Ce contributed to the electron transfer between MnO<sub>x</sub> and CeO<sub>x</sub> and promoted the migration of surface oxygen or lattice oxygen, (Geng et al. 2020) consequently improving the reduction performance of MnO<sub>x</sub> (Wang et al. 2013). Note that the peak at 466 °C corresponded to the reduction of CeO<sub>2</sub> on the catalyst surface to Ce<sub>2</sub>O<sub>3</sub> (Zhao et al. 2019).

XPS was used to characterize the surface properties of the TiMn15-NS and TiMn15Ce30-NS. Fig. 6a showed the Mn 2p spectrum of the catalysts, the peaks observed at 641.8 eV and 653.3 eV corresponded to Mn<sup>3+</sup>, and the peaks at 643.1 eV and 654.7 eV were attributed to Mn<sup>4+</sup> (Ferrel-Álvarez et al. 2018). It is widely established that the higher ratio of Mn<sup>4+</sup> can introduce more available oxygen species (Wang et al. 2013) and facilitate the redox cycling during reaction processes, which could promote catalytic activity

(Geng et al. 2020). The relative surface  $Mn^{4+}$  ratio calculated by  $Mn^{4+}/(Mn^{3+}+Mn^{4+})$  was displayed in Table 2, the surface  $Mn^{4+}$  content on TiMn15-NS was 65.8%, the value increased to 76.7% with introducing Ce. The phenomenon further elucidated that the addition of Ce was favorable for the electron transformation between Ce and Mn through the equilibrium of " $Mn^{3+} + Ce^{4+} \leftrightarrow Mn^{4+} + Ce^{3+}$ " (Wang et al. 2020a).

Table 2  
Surface atomic ratios of Mn 2p, O1s in TiMn15-NS and TiMn15Ce30-NS.

Samples	Surface atomic ratio <sup>[a]</sup> (%)	
	$Mn^{4+}/(Mn^{3+}+Mn^{4+})$	$O_{\alpha}/(O_{\alpha}+O_{\beta})$
TiMn15-NS	65.8	34.1
TiMn15Ce30-NS	76.7	46.4

<sup>[a]</sup> Surface atomic ratios were calculated based on the peak areas of binding energy.

The O1s peaks can be deconvoluted into two parts (Fig. 6b): the binding energies at 528.1 eV - 531.2 eV corresponding to lattice oxygen  $O^{2-}$  (denoted as  $O_{\beta}$ ), and the one at 528.1 eV - 534.8 eV ascribing to the surface oxygen species (denoted as  $O_{\alpha}$ ), such as  $O^{-}$  from the defect-oxide or  $OH^{-}$  ascribed to the hydroxyl-like group (Chen et al. 2017). And the relative concentration of surface oxygen species was calculated by  $O_{\alpha}/(O_{\alpha}+O_{\beta})$  as listed in Table 2. The area ratio of  $O_{\alpha}/(O_{\alpha}+O_{\beta})$  in TiMn15Ce30-NS (46.4%) was higher than that in TiMn15-NS (34.1%), indicating that the addition of Ce increased the concentration of reactive oxygen species.

## 3.2. Catalytic performance of the prepared catalysts in *o*-DCB oxidation

The conversion of *o*-DCB as a function of temperature over  $TiO_2$ -NTO,  $TiO_2$ -NS, TiMn15-NS and TiMn15-NTO were shown in Fig. 7. It can be seen that the activity of  $TiO_2$ -NS was higher than that of  $TiO_2$ -NTO in the entire temperature range. For example, the *o*-DCB conversion rate of  $TiO_2$ -NS was 38.2% at 350 °C, which was much higher than 15.6% of  $TiO_2$ -NTO, suggesting that the crystal plane of  $TiO_2$  significantly affected the activity of *o*-DCB oxidation, and the fact that  $TiO_2$ -NS with preferentially exposed {001} facet exhibited good catalytic activity could be explained by the abundant amount of unsaturated coordinated Ti atoms on the {001} crystal plane favoured high chemical activity, favouring the *o*-DCB adsorption and oxidation (Liu et al. 2016). The above result is in agreement with our previous study (Wen et al. 2021).  $TiO_2$ -NS doped with different amount of Mn or Ce were investigated. As illustrated in Fig. S3, the  $TiO_2$ -NS with 15 mol% of Mn/(Ti+Mn) exhibited the catalytic performance for *o*-DCB oxidation. Therefore, TiMn15-NS and TiMn15-NTO were synthesized and investigated. As obtained in Fig. 7, TiMn15-NS still presented superior activity with the  $T_{50\%}$  of 234 °C than that of 266 °C in TiMn15-NTO.

Moreover, the oxidation activity of TiMn15-NS was further improved when doping with 30 mol% of Ce in TiMn15Ce30-NS as suggested in Fig. S3. Similarly, TiMn15Ce30-NS also exhibited better oxidation activity than TiMn15Ce30-NTO (Fig. 8). For instance, the  $T_{50\%}$  of TiMn15Ce30-NS was 156 °C, and the value was 213 °C for TiMn15Ce30-NTO. These results further confirmed the influence of the crystal plane of  $\text{TiO}_2$  on *o*-DCB decomposition, which be closely associated with the preferentially exposed {001} crystal plane of TiMn15Ce30-NS (Wen et al. 2021). In addition, based on the results in Fig. 7 and Fig. 8, it showed that introduction of  $\text{CeO}_x$  on both TiMn15-NS and TiMn15-NTO significantly increased the activity for *o*-DCB oxidation. Especially for the TiMn15Ce30-NS, it exhibited excellent low temperature catalytic activity than TiMn15Ce30-NTO. Given the results mentioned above, the excellent catalytic activity of TiMn15Ce30 for *o*-DCB decomposition could be explained as follows. On the one hand, TiMnCe-NS with preferential exposed {001} crystal plane has more oxygen vacancies (Li et al. 2019b), which could enhance the activation of the active oxygen species and provide more adsorption sites for gas molecules (Liu et al. 2009). On another aspect, the strong interaction between  $\text{MnO}_x$  and  $\text{CeO}_x$  occurred in TiMnCe-NS, (Wang et al. 2020a) and hence the low-temperature reducibility of  $\text{MnO}_x$  was improved (Wang et al. 2013). In addition, TiMn15Ce30-NS possessed a higher content of  $\text{Mn}^{4+}$  and  $\text{O}_a$  than those of TiMn15-NS according to the XPS results due to the addition of Ce, which facilitated redox cycles between  $\text{Mn}^{3+}$  and  $\text{Ce}^{4+}$ , enhancing the migration of oxygen species (Wang et al. 2020a). Noteworthy, the current TiMn15Ce30-NS exhibited a significantly superior catalytic performance with the  $T_{90\%}$  of 238 °C compared with the TiFe5Ca70-S (322 °C) under the same space velocity condition, (Wen et al. 2021) suggesting that the catalytic activity of  $\text{MnCeO}_x/\text{TiO}_2$  for decomposing *o*-DCB could be further improved.

Water is an inevitable component in the actual flue gas, and the presence of water has an important effect on the catalytic oxidation for PCAHs (Ma et al. 2016). As shown in Fig. 8, in the presence of water (0.5 vol.%  $\text{H}_2\text{O}$ ), the activity of TiMn15Ce30-NS in the low-temperature region (< 200 °C) was inhibited to some extent, which was most likely ascribed to the competition adsorption between the  $\text{H}_2\text{O}$  and *o*-DCB on active sites of the catalyst surface (Hetrick et al. 2011). When the temperature was higher than 200 °C, the *o*-DCB conversion increased with the total conversion of *o*-DCB was still obtained at 300 °C. Moreover, the overall activity of TiMn15Ce30-NS with  $T_{50\%}$  of 179 °C and  $T_{90\%}$  of 240 °C was still clearly better than that of TiMn15Ce30-NTO with  $T_{50\%}$  of 205 °C and  $T_{90\%}$  of 246 °C under humid conditions. The above results suggested that the crystal plane also affected the catalytic performance of *o*-DCB oxidation in humid condition, (Wen et al. 2021) which might be explained by that the nanosheet morphology  $\text{TiO}_2$  {001} crystal surface allowed more hydroxyl groups to combine with the ortho Ti sites to generate more acidic sites (Wen et al. 2018) which could facilitate the adsorption of *o*-DCB (Li et al. 2021, Sun et al. 2016) and favor  $\text{H}_2\text{O}$  dissociation more easily compared with  $\text{TiO}_2$  {101} crystal surface (Vittadini et al. 1998), thus reducing the negative effect of competitive adsorption of  $\text{H}_2\text{O}$  and *o*-DCB.

The lifetime of TiMn15-NS, and TiMn15Ce30-NS for the *o*-DCB oxidation were evaluated at 350 °C (Fig. 9). TiMn15Ce30-NS catalyst exhibited excellent stability with *o*-DCB conversion retained at 98.9% for 12 h. However, for TiMn15-NS, the corresponding conversion decreased to 83.5%. The higher stability of TiMn15Ce30-NS could be also explained by its nanosheet structure with preferentially exposed {001} facet and the strong interaction among CeO<sub>2</sub>, MnO<sub>2</sub> and TiO<sub>2</sub>-NS support, thus reducing the adsorption of Cl<sup>-</sup> species on the active site of MnO<sub>x</sub> and CeO<sub>x</sub>, which is advantageous for chlorination species removal from the catalyst surface and maintain a relatively stable activity (Wang et al. 2014).

In brief, TiO<sub>2</sub> nanosheet supported MnCeO<sub>x</sub>/TiO<sub>2</sub> (TiMn15Ce30-NS) showed excellent low temperature catalytic activity, enhanced water resistance, and good stability for *o*-DCB oxidation, which was significantly better than most of the previous reported Mn-based catalysts (Table 3).

Table 3  
The states of the arts of Mn-based catalysts for PCAHs oxidation.

Catalysts	Pollutant	Reaction conditions	T <sub>50</sub> /T <sub>90</sub> (°C)	Ref.
TiMn15Ce30-NS	<i>o</i> -DCB	50 ppm, 10% O <sub>2</sub> /N <sub>2</sub> , 36000 mL·g <sup>-1</sup> ·h <sup>-1</sup>	156/238	<b>This work</b>
MnO <sub>x</sub> -D	<i>o</i> -DCB	1000 ppm, 20% O <sub>2</sub> /N <sub>2</sub> , 15000 mL·g <sup>-1</sup> ·h <sup>-1</sup>	238/321	(Ling et al. 2020)
CeMnO <sub>x</sub> -rod	<i>o</i> -DCB	1000 ppm, 20% O <sub>2</sub> /N <sub>2</sub> , 15000 mL·g <sup>-1</sup> ·h <sup>-1</sup>	293/346	(Zhao et al. 2019)
CeMn30	<i>o</i> -DCB	1000 ppm, 20% O <sub>2</sub> /N <sub>2</sub> , 15000 mL·g <sup>-1</sup> ·h <sup>-1</sup>	291/347	(Yang et al. 2019)
5.0%Ce/OMS	<i>o</i> -DCB	1000 ppm, 60000 mL·g <sup>-1</sup> ·h <sup>-1</sup>	>300/>335	(Chen et al. 2019)
Mn/Ce (0.50)	Chlorobenzene	1000 ppm, 20% O <sub>2</sub> /N <sub>2</sub> , 15000 h <sup>-1</sup>	165/231	(Hu et al. 2018)
15CM/TS-1.5	<i>o</i> -DCB	500 ppm, 20% O <sub>2</sub> /N <sub>2</sub> , 15000 mL·g <sup>-1</sup> ·h <sup>-1</sup>	>300/>360	(Zhao et al. 2018)
MCZ-0.67	Chlorobenzene	1000 ppm, 21% O <sub>2</sub> /N <sub>2</sub> , 20000 h <sup>-1</sup>	>175/226	(Zhu et al. 2019)
Mn-Ce-Zr ternary mixed oxides	<i>o</i> -DCB	1000 ppm, 21% O <sub>2</sub> /N <sub>2</sub> , 30000 h <sup>-1</sup>	>320/>390	(Long et al. 2019)
Mn-Ce-Fe	<i>o</i> -DCB	1000 ppm, 12000 mL·g <sup>-1</sup> ·h <sup>-1</sup>	253/380	(Tang et al. 2016)
30Cu/MnO <sub>x</sub>	Chlorobenzene	1000 ppm, 20% O <sub>2</sub> /N <sub>2</sub> , 15000 h <sup>-1</sup>	>150/290	(Chen et al. 2020)
MnO <sub>x</sub> /Co <sub>3</sub> O <sub>4</sub> -4h	Chlorobenzene	1000 ppm, 20% O <sub>2</sub> /N <sub>2</sub> , 60000 mL·g <sup>-1</sup> ·h <sup>-1</sup>	>275/>330	(Hu et al. 2021)
CoMn600@0.5Ti	Chlorobenzene	1000 ppm, 20% O <sub>2</sub> /N <sub>2</sub> , 15000 mL·g <sup>-1</sup> ·h <sup>-1</sup>	341/392	(Zhao et al. 2020a)

### 3.3. In situ FT-IR analysis of TiMn15Ce30-NS

Transient reaction processes characterized by in situ DRIFT spectra were performed to identify various reactive species and deduce a possible mechanism of the reaction. The DRIFT spectra collected at

different time intervals during the adsorption and oxidation of *o*-DCB over TiMn15Ce30-NS at 300 °C were shown in Fig. 10a. It can be seen that from 1 min to 30 min, no obvious change was observed in the range of 1000 ~ 2500 cm<sup>-1</sup>. The weak peak of 1283 cm<sup>-1</sup> (C-O stretching vibration) was assigned to the phenols (Lichtenberger 2004), the band at 1410 cm<sup>-1</sup> was associated with the formation of the *o*-benzoquinone (Lichtenberger 2004). It is widely accepted that the initial stage of *o*-DCB oxidation mainly includes the dissociative adsorption of *o*-DCB and nucleophilic substitution reaction. The lone pair electrons of the Cl atom are captured by the Lewis acid sites, causing a nucleophilic attack on the position of chlorine and breaking the C-Cl bonds, then *o*-DCB adsorbed on the active sites of transition metal oxides, generating phenolics via the reaction with surface oxygen (Lichtenberger 2004, Ma et al. 2013). Moreover, the *o*-DCB molecules can react at the Brønsted acid sites and produce HCl during the oxidation process according to Taralunga (Taralunga et al. 2006). Consequently, the characteristic peak of 1283 cm<sup>-1</sup> indicated that *o*-DCB was dechlorinated to form phenolics on the surface of TiMn15Ce30-NS, and the band at 1410 cm<sup>-1</sup> implied that the phenolics were further transformed into *o*-benzoquinone (Lichtenberger 2004). The band at 1374 cm<sup>-1</sup> corresponded to the symmetric -COO- stretching vibration of the surface formates species (Krishnamoorthy et al. 2000). The peaks at 1360 cm<sup>-1</sup> and 1540 cm<sup>-1</sup> were ascribed to the formation of carboxylates (acetates type) (Krishnamoorthy et al. 2000, Ma et al. 2016). Hence, it can be deduced that the *o*-benzoquinone was oxidized to formates and acetate over the TiMn15Ce30-NS. The weak peaks at 2320 cm<sup>-1</sup> and 2355 cm<sup>-1</sup> were assigned to the CO<sub>2</sub> (Silva et al. 2018), indicating that the intermediate formates and acetic species were further converted to CO<sub>2</sub> by deep oxidation. Besides, in addition to the intermediates mentioned above, the *o*-DCB catalyzed oxidation process is usually accompanied by the formation of H<sub>2</sub>O, which can be explained from our previous studies (Ma et al. 2019).

Figure 10b showed the in situ DRIFT spectra over TiMn15Ce30-NS collected at 100, 200, and 300 °C after 20 min reaction. As can be seen, the intensity of formates (1374 cm<sup>-1</sup>), acetates (1360 cm<sup>-1</sup>), and surface carbonates (1540 cm<sup>-1</sup>) were significantly enhanced when increasing the reaction temperature to 200 °C from 100 °C, demonstrating that the dechlorination, ring-opening and catalytic oxidation reactions took place over TiMn15Ce30-NS at 200 °C during *o*-DCB decomposition. When increasing the temperature to 300 °C, the intensity of formates, acetates, and surface carbonates all weakened obviously, meanwhile the peaks of CO<sub>2</sub> at 2320 cm<sup>-1</sup> and 2355 cm<sup>-1</sup> slightly increased. Therefore, it can be deduced that increasing temperature in a certain range (particularly from 200 to 300 °C) could promote the deep oxidation of *o*-DCB to CO<sub>2</sub> over TiMn15Ce30-NS.

Based on the mentioned above, the catalytic oxidation mechanism of *o*-DCB over TiMn15Ce30-NS can be elucidated in Fig. 11. As reported in previous reports (Mahmood et al. 2019), TiO<sub>2</sub> {001} crystal planes endow abundant 5-fold under-coordinated Ti atoms and 2-fold coordinated oxygen sites which were proved to be the adsorption active sites, we hence deduce that the *o*-DCB was prone to adsorbed on the {001} facet of TiMn15Ce30-NS. Subsequently, the adsorbed *o*-DCB transformed into phenolic species and then *o*-benzoquinone through nucleophilic substitution. Afterward, formates and acetate species were

formed via a ring-opening reaction of *o*-benzoquinone, and these species were finally oxidized to CO<sub>2</sub> and H<sub>2</sub>O.

## 4. Conclusions

Morphology engineered TiO<sub>2</sub>-NS and TiO<sub>2</sub>-NTO supported MnCeO<sub>x</sub> in *o*-DCB oxidation was investigated. TiMn15Ce30-NS exhibited better low temperature catalytic activity with T<sub>50%</sub> = 156 °C, T<sub>90%</sub> = 238 °C comparing with T<sub>50%</sub> = 213 °C and T<sub>90%</sub> = 247 °C for TiMn15Ce30-NTO. TiMn15Ce30-NS also showed superior water resistance (T<sub>50%</sub> = 179 °C, T<sub>90%</sub> = 240 °C), as well as excellent stability with the *o*-DCB oxidation conversion above 98% for 12 h at 350 °C, which verified the crucial influence of preferentially exposed {001} plane on *o*-DCB oxidation. The good catalytic performance of TiMn15Ce30-NS could be explained by the morphology engineering that improved its reducibility, surface oxygen species concentration, and higher ratio of Mn<sup>4+</sup>. This work provided an important clue for catalyst design through morphology engineering.

## Declarations

### Acknowledgment

The authors gratefully acknowledge financial supports from the Ministry of Science and Technology of China (Grant 2020YFC1808603), National Natural Science Foundation of China (Grants 21876042, 22020102004, 22108058 and 22106036), Natural Science Foundation of Hebei Province (Grants B2019202200, B2020202057, 21374204D and B2020202061).

### Ethics approval and consent to participate

This manuscript does not contain any studies with human participants or animals performed by any of the authors.

### Consent for publication

All authors give consent to publish the research in Environmental Science and Pollution Research.

### Availability of data and material

All relevant data generated or analyzed during this study were included in this published article.

### Competing interests

The authors declare that they have no competing interests.

### Funding

The authors gratefully acknowledge financial supports from the Ministry of Science and Technology of China (Grant 2020YFC1808603), National Natural Science Foundation of China (Grants 21876042, 22020102004, 22108058 and 22106036), Natural Science Foundation of Hebei Province (Grants B2019202200, B2020202057, 21374204D and B2020202061).

### Author's contributions

Xu He: Investigation, Conceptualization, Experimental, Data Curation, Formal analysis, Writing-Original Draft. Haiwei Guo: Conceptualization, Validation, Formal analysis, Writing-Review & Editing. Xiaoyao Liu: Methodology, Investigation, Experimental. Jiaxin Wen: Software, Visualization, Data curation. Gengbo Ren: Methodology, Investigation, Validation. Xiaodong Ma: Writing-Review & Editing, Supervision, Project administration, Funding acquisition.

All authors read and approved the final manuscript.

## References

1. Abebe B, Murthy HCA, Amare E (2018) Summary on adsorption and photocatalysis for pollutant remediation: Mini review. *J Encapsulation Adsorpt Sci* 08:225–255. <https://doi.org/10.4236/jeas.2018.84012>
2. Arandiyani H, Wang Y, Sun HY, Rezaei M, Dai HX (2018) Ordered meso- and macroporous perovskite oxide catalysts for emerging applications. *Chem Commun* 54:6484–6502. <https://doi.org/10.1039/C8CC01239C>
3. Cao YJ, Cui Z, Ji T, Li WY, Xu KB, Zou R, Yang JM, Qin ZY, Hu JQ (2017) Hierarchical MoO<sub>3</sub>/MnO<sub>2</sub> core-shell nanostructures with enhanced pseudocapacitive properties. *J Alloys Compd* 725:373–378. <https://doi.org/10.1016/j.jallcom.2017.07.182>
4. Chen HF, Xia Y, Huang H, Gan YP, Tao XY, Liang C, Luo JM, Fang RY, Zhang J, Zhang WK, Liu XS (2017) Highly dispersed surface active species of Mn/Ce/TiW catalysts for high performance at low temperature NH<sub>3</sub>-SCR. *Chem Eng J* 330:1195–1202. <https://doi.org/10.1016/j.cej.2017.08.069>
5. Chen J, Chen X, Chen X, Xu WJ, Xu Z, Jia HP, Chen J (2018) Homogeneous introduction of CeO<sub>y</sub> into MnO<sub>x</sub>-based catalyst for oxidation of aromatic VOCs. *Appl Catal B-Environ* 224:825–835. <https://doi.org/10.1016/j.apcatb.2017.11.036>
6. Chen J, Chen X, Yan DX, Jiang MZ, Xu WJ, Yu H, Jia HP (2019) A facile strategy of enhancing interaction between cerium and manganese oxides for catalytic removal of gaseous organic contaminants. *Appl Catal B-Environ* 250:396–407. <https://doi.org/10.1016/j.apcatb.2019.03.042>
7. Chen X, He F, Liu ST (2020) CuO/MnO<sub>x</sub> composites obtained from Mn-MIL-100 precursors as efficient catalysts for the catalytic combustion of chlorobenzene. *React Kinet Mech Cat* 130:1063–1076. <https://doi.org/10.1007/s11144-020-01816-6>

8. Deng SC, Meng TT, Xu BL, Gao F, Ding YH, Yu L, Fan YN (2016) Advanced  $\text{MnO}_x/\text{TiO}_2$  catalyst with preferentially exposed anatase {001} facet for low-temperature SCR of NO. *ACS Catal* 6:5807–5815. <https://doi.org/10.1021/acscatal.6b01121>
9. Deng W, Gao B, Jia Z, Liu DQ, Guo LM (2021) Co–Cr bimetallic oxides derived from layered double hydroxides with high catalytic performance for chlorinated aromatics oxidation. *Catal Sci Technol* 11:5094–5108. <https://doi.org/10.1039/d1cy00791b>
10. Ferrel-Álvarez AC, Domínguez-Crespo MA, Cong H, Torres-Huerta AM, Brachetti-Sibaja SB, De La Cruz W (2018) Synthesis and surface characterization of the  $\text{La}_{0.7-x}\text{Pr}_x\text{Ca}_{0.3}\text{MnO}_3$  (LPCM) perovskite by a non-conventional microwave irradiation method. *J Alloys Compd* 735:1750–1758. <https://doi.org/10.1016/j.jallcom.2017.11.306>
11. Geng LL, Chen BB, Yang JH, Shui CL, Ye SS, Fu JL, Zhang NW, Xie JR, Chen BH (2020) Synergistic effect between Mn and Ce for active and stable catalytic wet air oxidation of phenol over  $\text{MnCeO}_x$ . *Appl Catal A-Gen* 604: 117774. <https://doi.org/10.1016/j.apcata.2020.117774>
12. Yang HG, Liu G, Qiao SZ, Sun CH, Jin YG, Smith SC, Zou J, Cheng HM, Lu GQ (2009) Solvothermal synthesis and photoreactivity of anatase  $\text{TiO}_2$  nanosheets with dominant {001} facets. *J Am Chem Soc* 131. <https://doi.org/10.1021/ja808790p>
13. He C, Cheng J, Zhang X, Douthwaite M, Pattison S, Hao ZP (2019a) Recent advances in the catalytic oxidation of volatile organic compounds: A Review based on pollutant sorts and sources. *Chem Rev* 119:4471–4568. <https://doi.org/10.1021/acs.chemrev.8b00408>
14. He F, Jiao YM, Wu LY, Chen X, Liu ST (2019b) Enhancement mechanism of Sn on the catalytic performance of Cu/KIT-6 during the catalytic combustion of chlorobenzene. *Catal Sci Technol* 9:6114–6123. <https://doi.org/10.1039/c9cy01169b>
15. Hetrick CE, Patcas F, Amiridis MD (2011) Effect of water on the oxidation of dichlorobenzene over  $\text{V}_2\text{O}_5/\text{TiO}_2$  catalysts. *Appl Catal B-Environ* 101:622–628. <https://doi.org/10.1016/j.apcatb.2010.11.003>
16. Hu WK, He F, Chen X, Liu ST (2018) Hydrothermal synthesis of leaf-like  $\text{CeO}_2$  nanosheets and its  $\text{MnO}_x/\text{CeO}_2$  composites for catalytic combustion of chlorobenzene. *J Nanopart Res* 21:1–14. <https://doi.org/10.1007/s11051-018-4441-x>
17. Hu ZY, Chen J, Yan DX, Li Y, Jia HP, Lu CZ (2021) Enhanced catalytic activities of  $\text{MnO}_x/\text{Co}_3\text{O}_4$  nanocomposites prepared via MOFs-templated approach for chlorobenzene oxidation. *Appl Surf Sci* 551:149453. <https://doi.org/10.1016/j.apsusc.2021.149453>
18. Jiao YM, Chen X, He F, Liu ST (2019) Simple preparation of uniformly distributed mesoporous Cr/ $\text{TiO}_2$  microspheres for low-temperature catalytic combustion of chlorobenzene. *Chem Eng J* 372:107–117. <https://doi.org/10.1016/j.cej.2019.04.118>
19. Khan WU, Chen SS, Tsang DCW, Teoh WY, Hu X, Lam FLY, Yip ACK (2020) Catalytically active interfaces in titania nanorod-supported copper catalysts for CO oxidation. *Nano Res* 13:533–542. <https://doi.org/10.1007/s12274-020-2647-6>

20. Krishnamoorthy S, Rivas JA, Amiridis MD (2000) Catalytic oxidation of 1,2-dichlorobenzene over supported transition metal oxides. *J Catal* 193:264–272. <https://doi.org/10.1006/jcat.2000.2895>
21. Leng YP, Gao YH, Wang WC, Zhao YP (2015) Continuous supercritical solvothermal synthesis of TiO<sub>2</sub>-pristine-graphene hybrid as the enhanced photocatalyst. *J Super Crit Fluid* 103:115–121. <https://doi.org/10.1016/j.supflu.2015.05.001>
22. Li GB, Shen K, Wang L, Zhang YP, Yang HQ, Wu P, Wang B, Zhang SL (2021) Synergistic degradation mechanism of chlorobenzene and NO over the multi-active center catalyst: The role of NO<sub>2</sub>, Brønsted acidic site, oxygen vacancy. *Appl Catal B-Environ* 286:119865. <https://doi.org/10.1016/j.apcatb.2020.119865>
23. Li P, Chen X, Li Y, Schwank JW (2019a) A review on oxygen storage capacity of CeO<sub>2</sub>-based materials: Influence factors, measurement techniques, and applications in reactions related to catalytic automotive emissions control. *Catal Today* 327:90–115. <https://doi.org/10.1016/j.cattod.2018.05.059>
24. Li Q, Li X, Li W, Zhong L, Zhang C, Fang QY, Chen G (2019b) Effect of preferential exposure of anatase TiO<sub>2</sub>{001} facets on the performance of Mn-Ce/TiO<sub>2</sub> catalysts for low-temperature selective catalytic reduction of NO<sub>x</sub> with NH<sub>3</sub>. *Chem Eng J* 369:26–34. <https://doi.org/10.1016/j.cej.2019.03.054>
25. Li Y, Guo YY, Zhu TY, Ding S (2016) Adsorption and desorption of SO<sub>2</sub>, NO and chlorobenzene on activated carbon. *J Environ Sci* 43:128–135. <https://doi.org/10.1016/j.jes.2015.08.022>
26. Li ZM, Guo XL, Tao F, Zhou RX (2018) New insights into the effect of morphology on catalytic properties of MnO<sub>x</sub>-CeO<sub>2</sub> mixed oxides for chlorobenzene degradation. *RSC Adv* 8:25283–25291. <https://doi.org/10.1039/c8ra04010a>
27. Lichtenberger J (2004) Catalytic oxidation of chlorinated benzenes over V<sub>2</sub>O<sub>5</sub>/TiO<sub>2</sub> catalysts. *J Catal* 223:296–308. <https://doi.org/10.1016/j.jcat.2004.01.032>
28. Lindberg D, Molin C, Hupa M (2015) Thermal treatment of solid residues from WtE units: a review. *Waste manage* 37:82–94. <https://doi.org/10.1016/j.wasman.2014.12.009>
29. Ling WT, Zhao HJ, Tang ZC, Zha F (2020) Direct synthesis of novel sponge-like porous MnO<sub>x</sub> catalysts derived from Mn-MOFs for high-efficiently eliminate *o*-dichlorobenzene by catalytic combustion. *Catal Surv Asia* 24:278–290. <https://doi.org/10.1007/s10563-020-09308-2>
30. Liu F, He H (2010) Structure-activity relationship of iron titanate catalysts in the selective catalytic reduction of NO<sub>x</sub> with NH<sub>3</sub>. *J Phys Chem C* 114:16929–16936
31. Liu N, Li K, Li X, Chang Y, Feng YL, Sun XJ, Cheng Y, Wu ZJ, Zhang HY (2016) Crystallographic facet-induced toxicological responses by faceted titanium dioxide nanocrystals. *ACS Nano* 10:6062–6073. <https://doi.org/10.1021/acsnano.6b01657>
32. Liu XG, Zhou KB, Wang L, Wang BY, Li YD (2009) Oxygen vacancy clusters promoting reducibility and activity of ceria nanorods. *J Am Chem Soc* 131:3140–3141. <https://doi.org/10.1021/ja808433d>

33. Liu Y, Luo MF, Wei ZB, Xin Q, Ying PL, Li C (2001) Catalytic oxidation of chlorobenzene on supported manganese oxide catalysts. *Appl Catal B-Environ* 29:61–67. [https://doi.org/10.1016/S0926-3373\(00\)00193-4](https://doi.org/10.1016/S0926-3373(00)00193-4)
34. Long GY, Chen MX, Li YJ, Ding JF, Sun RZ, Zhou YF, Huang XY, Han GR, Zhao WR (2019) One-pot synthesis of monolithic Mn-Ce-Zr ternary mixed oxides catalyst for the catalytic combustion of chlorobenzene. *Chem Eng J* 360:964–973. <https://doi.org/10.1016/j.cej.2018.07.091>
35. Ma XD, Sun Q, Feng X, He X, Guo J, Sun HW, Cao HQ (2013) Catalytic oxidation of 1,2-dichlorobenzene over  $\text{CaCO}_3/\alpha\text{-Fe}_2\text{O}_3$  nanocomposite catalysts. *Appl Catal A-Gen* 450:143–151. <https://doi.org/10.1016/j.apcata.2012.10.019>
36. Ma XD, Feng X, Guo J, Cao HQ, Suo XY, Sun HW, Zheng MH (2014) Catalytic oxidation of 1,2-dichlorobenzene over Ca-doped  $\text{FeO}_x$  hollow microspheres. *Appl Catal B-Environ* 147:666–676. <https://doi.org/10.1016/j.apcatb.2013.10.003>
37. Ma XD, Zhao MY, Pang Q, Zheng MH, Sun HW, Crittenden J, Zhu YY, Chen YS (2016) Development of novel  $\text{CaCO}_3/\text{Fe}_2\text{O}_3$  nanorods for low temperature 1,2-dichlorobenzene oxidation. *Appl Catal A-Gen* 522:70–79. <https://doi.org/10.1016/j.apcata.2016.04.025>
38. Ma XD, Wen JX, Guo HW, Ren GB (2019) Facile template fabrication of Fe-Mn mixed oxides with hollow microsphere structure for efficient and stable catalytic oxidation of 1,2-dichlorobenzene. *Chem Eng J* 122940. <https://doi.org/10.1016/j.cej.2019.122940>
39. Mahmood A, Shi GS, Xie XF, Sun J (2019) Adsorption mechanism of typical oxygen, sulfur, and chlorine containing VOCs on  $\text{TiO}_2(001)$  surface: First principle calculations. *Appl Surf Sci* 471:222–230. <https://doi.org/10.1016/j.apsusc.2018.12.017>
40. Martra G (2000) Lewis acid and base sites at the surface of microcrystalline  $\text{TiO}_2$  anatase: relationships between surface morphology and chemical behaviour. *Appl Catal A-Gen* 200:275–285
41. Qiu J, Peng YQ, Tang MH, Lu SY, Li XD, Yan JH (2021) Catalytic activity, selectivity, and stability of co-precipitation synthesized Mn-Ce mixed oxides for the oxidation of 1,2-dichlorobenzene. *Environ Sci Pollut Res* 28:65416–65427. <https://doi.org/10.1007/s11356-021-15016-9>
42. Rahman M, Pal, Shafiullah S (2019) A statistical approach to determine optimal models for IUPAC-classified adsorption isotherms. *Energies* 12:4565. <https://doi.org/10.3390/en12234565>
43. Silva LPC, Freitas MM, Santos RM, Perez G, Terra LE, Coutinho ACSLS, Passos FB (2018) The effect of metal type on the sulfur tolerance of catalysts supported on niobia for sour water-gas shift reaction. *Int J Hydrogen Energy* 43:3190–3202. <https://doi.org/10.1016/j.ijhydene.2017.12.144>
44. Sun PF, Wang WL, Dai XX, Weng XL, Wu ZB (2016) Mechanism study on catalytic oxidation of chlorobenzene over  $\text{Mn}_x\text{Ce}_{1-x}\text{O}_2/\text{H-ZSM5}$  catalysts under dry and humid conditions. *Appl Catal B-Environ* 198:389–397. <https://doi.org/10.1016/j.apcatb.2016.05.076>
45. Tang AD, Hu LQ, Yang XH, Jia YR, Zhang Y (2016) Promoting effect of the addition of Ce and Fe on manganese oxide catalyst for 1,2-dichlorobenzene catalytic combustion. *Catal Commun* 82:41–45. <https://doi.org/10.1016/j.catcom.2016.04.015>

46. Taralunga M, Mijoin J, Magnoux P (2006) Catalytic destruction of 1,2-dichlorobenzene over zeolites. *Catal Commun* 7:115–121. <https://doi.org/10.1016/j.catcom.2005.09.006>
47. Van den Brink RW, Krzan M, Feijen-Jeurissen MMR, Louw R, Mulder P (2000) The role of the support and dispersion in the catalytic combustion of chlorobenzene on noble metal based catalysts. *Appl Catal B-Environ* 24:255–264. [https://doi.org/https://doi.org/10.1016/S0926-3373\(99\)00113-7](https://doi.org/https://doi.org/10.1016/S0926-3373(99)00113-7)
48. Vittadini A, Selloni A, Rotzinger FP, M. G (1998) Structure and energetics of water adsorbed at TiO<sub>2</sub> anatase (101) and (001) surfaces. *Physical Review Letter* 81:2954–2957
49. Wang QL, Zhou JJ, Zhang JC, Zhu H, Feng YH, Jin J (2020a) Effect of ceria doping on catalytic activity and SO<sub>2</sub> resistance of MnO<sub>x</sub>/TiO<sub>2</sub> catalysts for selective catalytic reduction of NO with NH<sub>3</sub> at low temperature. *Aerosol Air Qual Res* 20:477–488. <https://doi.org/10.4209/aaqr.2019.10.0546>
50. Wang T, Xiao H, Gao Y, Xu J, Zhang ZM, Bian HQ, Sun TY (2020b) Ag<sub>2</sub>O/TiO<sub>2</sub> hollow microsphere heterostructures with exposed high-energy {001} crystal facets and high photocatalytic activities. *J Materials Sci-Mater El* 31:11496–11507. <https://doi.org/10.1007/s10854-020-03697-w>
51. Wang XY, Ran L, Dai Y, Lu YJ, Dai QG (2014) Removal of Cl adsorbed on Mn-Ce-La solid solution catalysts during CVOC combustion. *J Colloid Interface Sci* 426:324–332. <https://doi.org/10.1016/j.jcis.2013.10.007>
52. Wang Z, Shen GL, Li JQ, Liu HD, Wang Q, Chen YF (2013) Catalytic removal of benzene over CeO<sub>2</sub>-MnO<sub>x</sub> composite oxides prepared by hydrothermal method. *Appl Catal B-Environ* 138–139:253–259. <https://doi.org/10.1016/j.apcatb.2013.02.030>
53. Wen JX, Guo HW, He X, Tong X, Gao P, Dong QX, Ren GB, Ma XD (2021) Morphology-engineering enhanced catalytic performance improvement of Fe-Ca-O<sub>x</sub>/TiO<sub>2</sub> for 1,2-dichlorobenzene oxidation. *Appl Catal A-Gen* 613:118030. <https://doi.org/10.1016/j.apcata.2021.118030>
54. Wen YX, Cao S, Fei XQ, Wang HQ, Wu ZB (2018) One-step synthesized SO<sub>4</sub><sup>2-</sup>-TiO<sub>2</sub> with exposed (001) facets and its application in selective catalytic reduction of NO by NH<sub>3</sub>. *Chin J Catal* 39:771–778. [https://doi.org/10.1016/s1872-2067\(18\)63034-7](https://doi.org/10.1016/s1872-2067(18)63034-7)
55. Weng XL, Long Y, Wang WL, Shao M, Wu ZB (2019) Structural effect and reaction mechanism of MnO<sub>2</sub> catalysts in the catalytic oxidation of chlorinated aromatics. *Chin J Catal* 40:638–646. [https://doi.org/10.1016/s1872-2067\(19\)63322-x](https://doi.org/10.1016/s1872-2067(19)63322-x)
56. Wu LY, He F, Luo JQ, Liu ST (2017) Synthesis of three-dimensional ordered mesoporous MnO<sub>x</sub>/CeO<sub>2</sub> bimetal oxides for the catalytic combustion of chlorobenzene. *RSC Adv* 7:26952–26959. <https://doi.org/10.1039/c7ra02299a>
57. Wu XM, Yu XL, Huang ZW, Shen HZ, Jing GH (2019) MnO<sub>x</sub>-decorated VO<sub>x</sub>/CeO<sub>2</sub> catalysts with preferentially exposed {110} facets for selective catalytic reduction of NO<sub>x</sub> by NH<sub>3</sub>. *Appl Catal B-Environ*: 118419. <https://doi.org/10.1016/j.apcatb.2019.118419>
58. Yang S, Zhao HJ, Dong F, Zha F, Tang ZC (2019) Highly efficient catalytic combustion of *o*-dichlorobenzene over three-dimensional ordered mesoporous cerium manganese bimetallic oxides: A

- new concept of chlorine removal mechanism. *Molecular Catalysis* 463:119–129.  
<https://doi.org/10.1016/j.mcat.2018.12.006>
59. Zhang Z, Huang J, Xia HQ, Dai QG, Gu YF, Lao YJ, Wang XY (2018) Chlorinated volatile organic compound oxidation over  $\text{SO}_4^{2-}/\text{Fe}_2\text{O}_3$  catalysts. *J Catal* 360:277–289.  
<https://doi.org/10.1016/j.jcat.2017.11.024>
60. Zhao HJ, Han WL, Dong F, Tang ZC (2018) Highly-efficient catalytic combustion performance of 1,2-dichlorobenzene over mesoporous  $\text{TiO}_2\text{-SiO}_2$  supported CeMn oxides: The effect of acid sites and redox sites. *J Ind Eng Chem* 64:194–205. <https://doi.org/10.1016/j.jiec.2018.03.016>
61. Zhao HJ, Dong F, Han WL, Tang ZC (2019) Study of morphology-dependent and crystal-plane effects of  $\text{CeMnO}_x$  catalysts for 1,2-dichlorobenzene catalytic elimination. *Ind Eng Chem Res* 58:18055–18064. <https://doi.org/10.1021/acs.iecr.9b02138>
62. Zhao HJ, Han WL, Tang ZC (2020a) Tailored design of high-stability  $\text{CoMn}_{1.5}\text{O}_x@ \text{TiO}_2$  double-wall nanocages derived from prussian blue analogue for catalytic combustion of *o*-dichlorobenzene. *Appl Catal B-Environ* 276:119133. <https://doi.org/10.1016/j.apcatb.2020.119133>
63. Zhao H, Li HC, Pan ZF, Feng F, Gu YW, Du JC, Zhao YK (2020b) Design of CeMnCu ternary mixed oxides as soot combustion catalysts based on optimized Ce/Mn and Mn/Cu ratios in binary mixed oxides. *Appl Catal B-Environ* 268:118422. <https://doi.org/10.1016/j.apcatb.2019.118422>
64. Zhu L, Li X, Liu ZY, Yao L, Yu P, Wei P, Xu YH, Jiang XM (2019) High catalytic performance of Mn-doped Ce-Zr catalysts for chlorobenzene elimination. *Nanomaterials* 9:1–19.  
<https://doi.org/10.3390/nano9050675>

## Figures

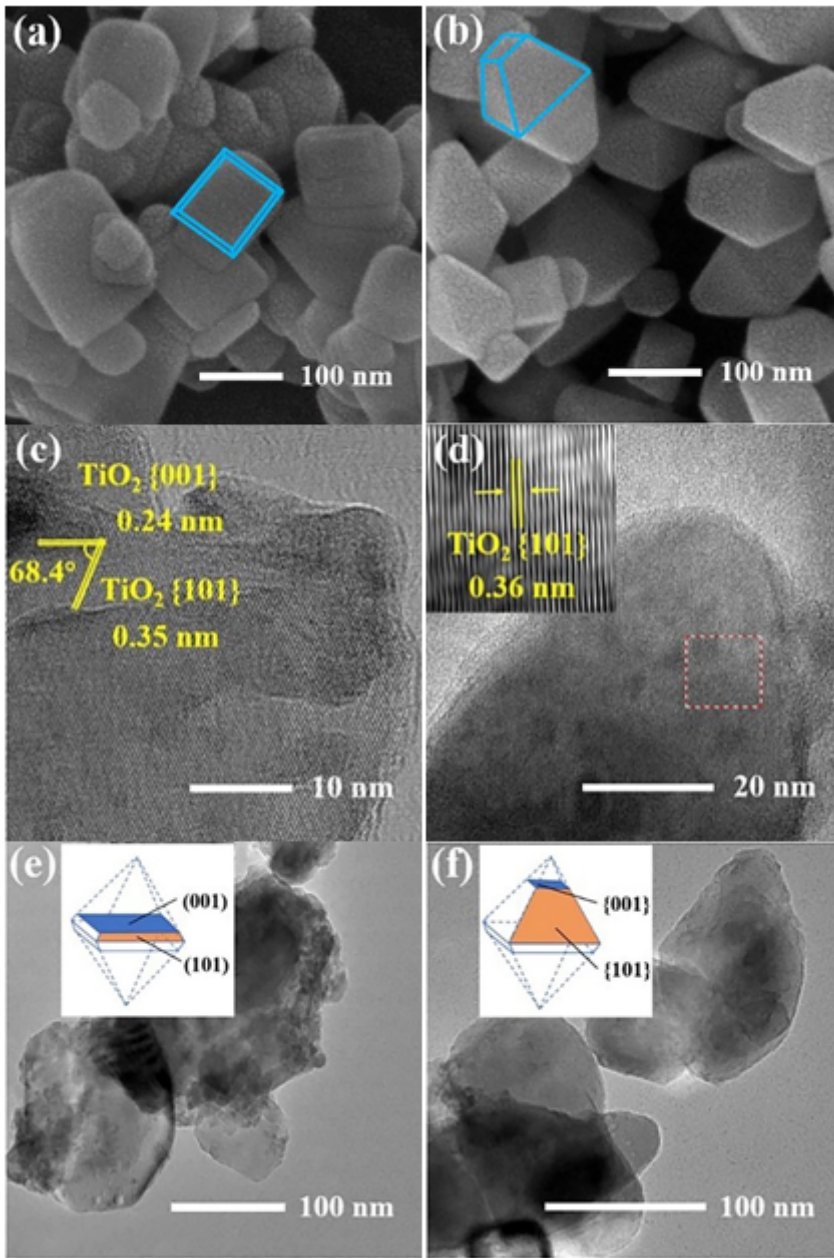


**Figure 1**

SEM images of (a)  $\text{TiO}_2$ -NS, (b)  $\text{TiO}_2$ -NTO, HRTEM images of (c)  $\text{TiMn}_{15}\text{Ce}_{30}$ -NS, (d)  $\text{TiMn}_{15}\text{Ce}_{30}$ -NTO and TEM images of (e)  $\text{TiMn}_{15}\text{Ce}_{30}$ -NS, (f)  $\text{TiMn}_{15}\text{Ce}_{30}$ -NTO.

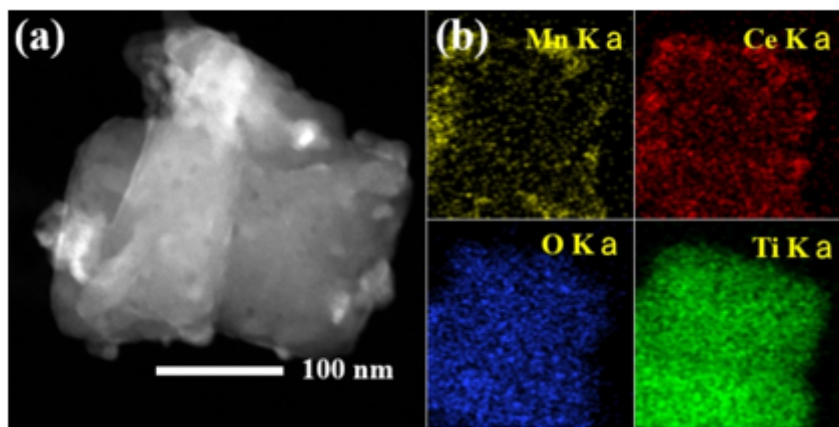


Figure 2

(a) The TEM and (b) the energy dispersive spectroscopy elemental mapping of TiMn15Ce30-NS.

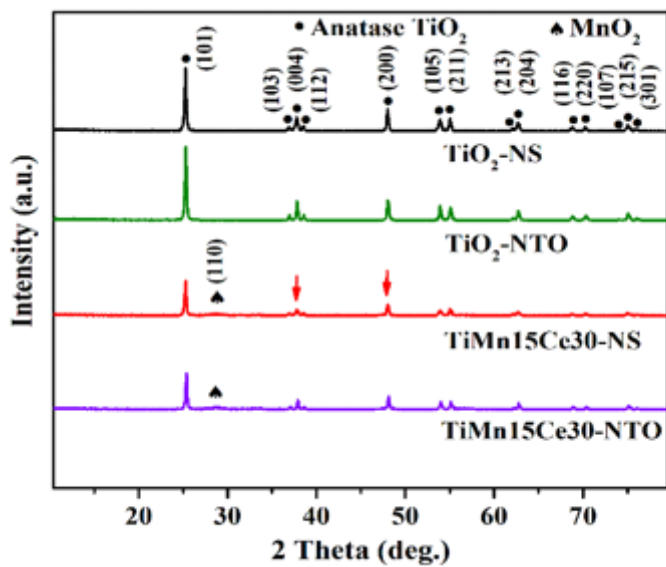


Figure 3

XRD patterns of TiO<sub>2</sub>-NS, TiO<sub>2</sub>-NTO, TiMn15Ce30-NS and TiMn15Ce30-NTO.

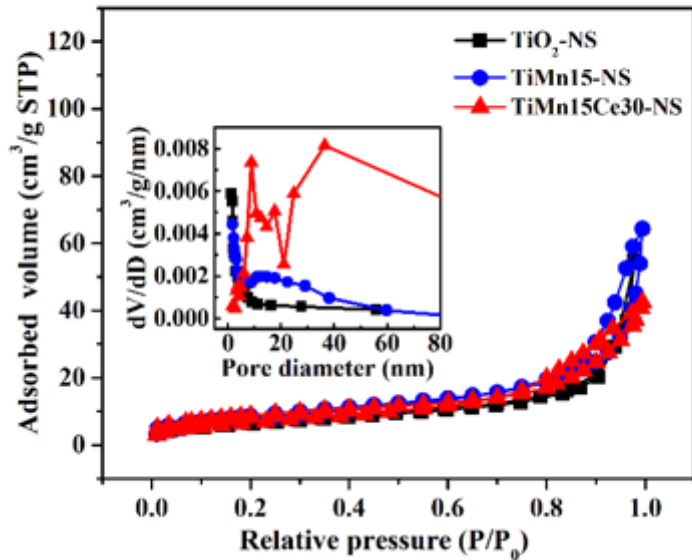


Figure 4

The  $N_2$  adsorption/desorption isotherms and pore size distribution of  $TiO_2$ -NS, TiMn15-NS and TiMn15Ce30-NS.

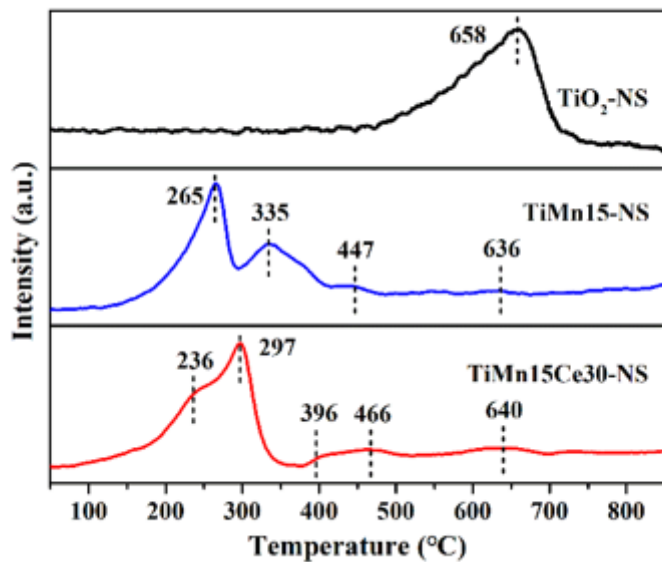


Figure 5

$H_2$ -TPR profiles of  $TiO_2$ -NS, TiMn15-NS and TiMn15Ce30-NS.

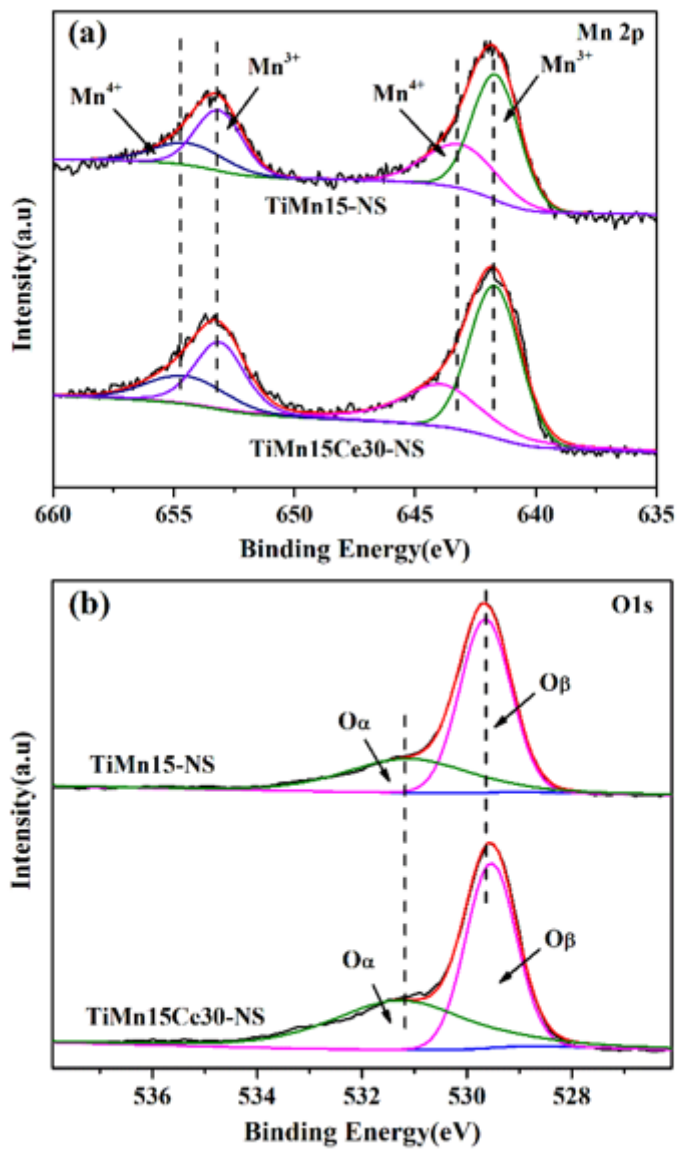


Figure 6

XPS profiles of TiMn15-NS and TiMn15Ce30-NS (a) Mn 2p, (b) O 1s.

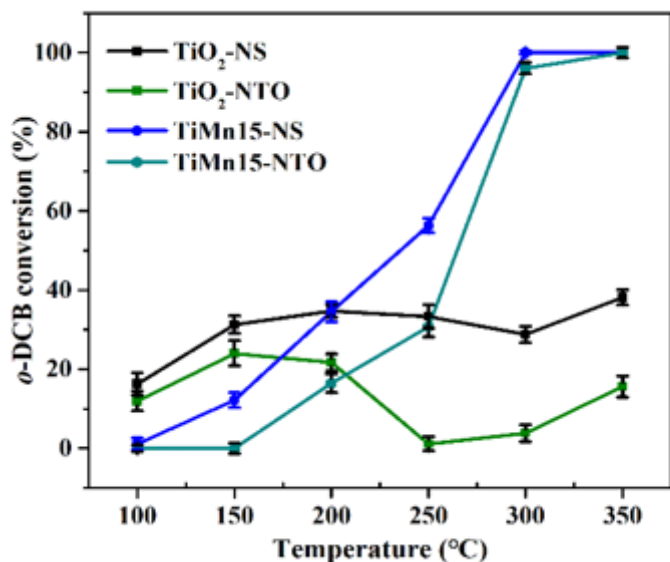


Figure 7

Light-off curves for the catalytic oxidation of *o*-DCB over TiO<sub>2</sub>-NS and TiO<sub>2</sub>-NTO and TiMn15-NS and TiMn15-NTO. (50 ppm DCB, 10% O<sub>2</sub>, WHSV = 36,000 mL/(g·h)).

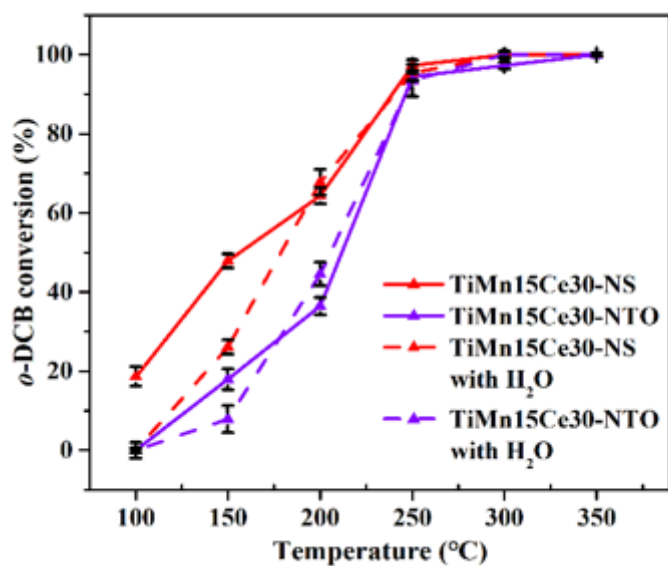


Figure 8

Light-off curves for the catalytic oxidation of *o*-DCB over TiMn15Ce30-NS and TiMn15Ce30-NTO in dry and humid condition (0.5 vol% H<sub>2</sub>O). (50 ppm DCB, 10% O<sub>2</sub>, WHSV = 36,000 mL/(g·h)).

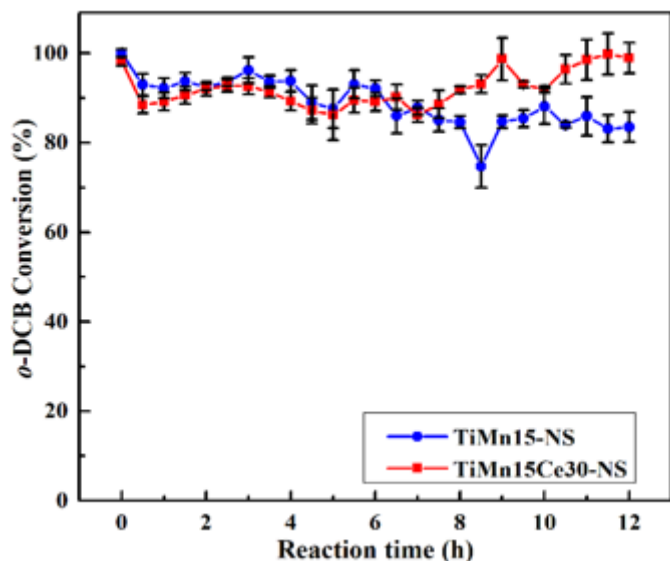


Figure 9

The stability tests of TiMn15-NS and TiMn15Ce30-NS at 350 °C (50 ppm *o*-DCB, 10% O<sub>2</sub>, WHSV = 36,000 mL·g<sup>-1</sup>·h<sup>-1</sup>).

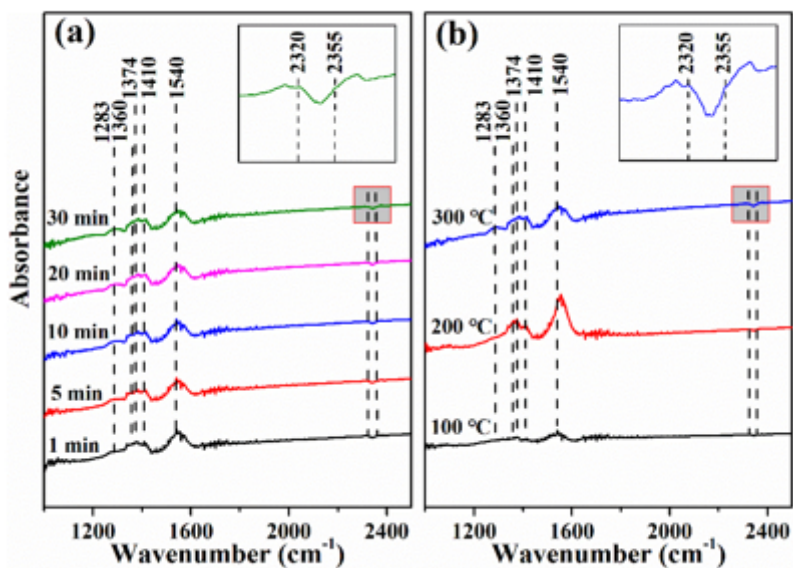


Figure 10

In situ DFIRTS spectra of TiMn15Ce30-NS: (a) 1, 5, 10, 20 and 30 min at 300 °C and (b) 100, 200 and 300 °C at 20 min.

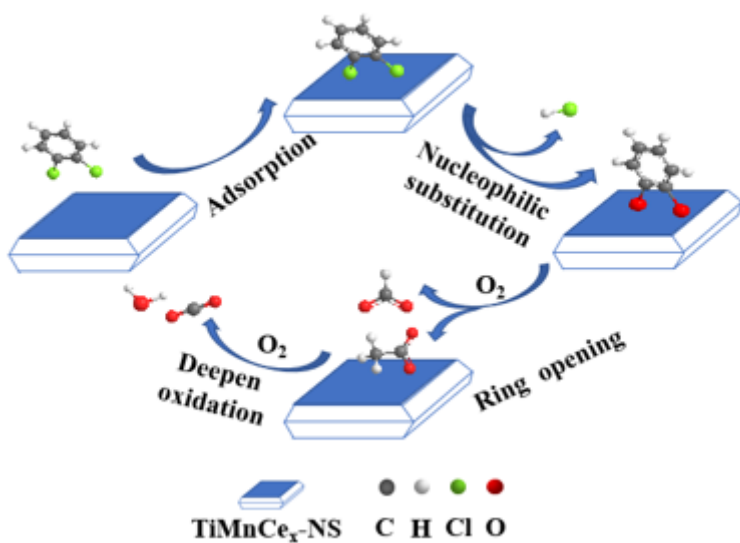


Figure 11

Proposed mechanism for *o*-DCB oxidation over TiMn<sub>15</sub>Ce<sub>30</sub>-NS.

## Supplementary Files

This is a list of supplementary files associated with this preprint. Click to download.

- [Supportinginformation.docx](#)